Boron kagome-layer induced intrinsic superconductivity in a MnB_3 monolayer with a high critical temperature

Ziyang Qu,[1,*] Fanjunjie Han,[2,*] Tong Yu,[2] Meiling Xu,[1,†] Yinwei Li,[1,‡] and Guochun Yang[2,§]

[1]*Laboratory of Quantum Materials Design and Application, School of Physics and Electronic Engineering, Jiangsu Normal University, Xuzhou 221116, China*

[2]*Centre for Advanced Optoelectronic Functional Materials Research and Key Laboratory for UV Light-Emitting Materials and Technology of Ministry of Education, Northeast Normal University, Changchun 130024, China*

(Received 26 May 2020; revised 5 July 2020; accepted 30 July 2020; published 14 August 2020)

The design of two-dimensional superconductors has attracted great research interest owing to their wide application in nanoscale devices. Here, we combine first-principles calculations with structure searching technology to identify a unique stable hexagonal h-MnB_3 monolayer, exhibiting a slightly higher energy with respect to the reported tetragonal t-MnB_3. Interestingly, h-MnB_3 contains two boron kagome layers sandwiched with Mn atoms. It exhibits metallic properties and has a superconducting transition temperature of 24.9 K, which is much higher than 2.9 K in t-MnB_3. Its superconductivity mainly originates from the coupling between in-plane vibrational phonons of boron kagome layers and electrons of Mn atoms. h-MnB_3 exhibits a tunable superconductivity, and reaches a maximum of 34 K at 2% tensile strain resulting from the softening in-plane modes of boron kagome layers. The Si (111) surface may be an ideal substrate for the growth of superconductive h-MnB_3. The unique superconducting mechanism observed here could inspire the searching of more boron kagome based two-dimensional superconductors.

DOI: 10.1103/PhysRevB.102.075431

I. INTRODUCTION

The search for superconductors near room temperature has long been viewed as a significant problem in condensed matter physics [1,2]. Recent theoretical predictions [3–6] and experimental observations [7–10] of high critical temperature (T_c) superconductivity in hydrogen-rich materials have achieved much success. Compared with bulk superconductors, two-dimensional (2D) superconducting materials play an irreplaceable role in nondissipative electronic devices, low-dissipative integrated circuits, smaller size, and higher precision measurement, as well as imaging equipment [11]. However, with respect to the huge 2D material family, the existing 2D superconducting materials are relatively limited [12–18]. On the other hand, their superconducting transition temperatures are low. Thus, it is urgent to develop new 2D superconducting materials with desirable properties.

Akin to hydrogen-rich superconductors at high pressures, the discovery of 2D superconductors was not serendipitous; both crystal structure prediction and first-principles calculations inspired experiment and helped to interpret the results [12,19,20]. It was theoretically proposed that superconductivity in graphene can be induced by alkali atom adsorption because of the enhanced electron-phonon coupling (EPC) [12]. Experimental investigations motivated by this result demonstrated that Li-decorated monolayer graphene is superconducting with a T_c of 5.9 K [19]. Theoretical studies have shown that ultrathin MgB_2 exhibits multigap superconductivity which originates from the surface states hybridizing with π bands of graphenelike boron layers [20]. Meanwhile, the theoretical predictions were validated by *in situ* angle-resolved photoemission spectroscopy in experiment [20].

Inspired by the boron-driven superconductivity in bulk and the fact that ultrathin MgB_2 and boron has a small atomic mass, the superconducting properties of pure boron material have been widely studied [21–26]. Theoretical studies suggested that most of the 2D boron allotropes (α [21,22,24], $B_{\diamond}$ [26], $B_{\square}$ [26] and buckled triangular sheets [26]) are phonon-mediated superconductors with T_c from 6.7 to 21 K. The superconductivity of these 2D boron allotropes mainly originates from the EPC between the out-of-plane vibration modes and π electrons near Fermi energy [27]. The relatively high T_c predicted in pure boron materials and accessibility of metal borides motivates the design of boron based 2D superconducting borides, such as MgB_6 [28], GaB_6 [29], InB_6 [29], Li_2B_7 [30] AlB_6 [31], and Mo_2B_2 [32]. All these 2D compounds contain boron hexagonal or triangular frameworks. Interestingly, boron atoms in MgB_6 form peculiar kagome lattices with each hexagon comprising edges of six atom-sharing triangles. EPC calculations demonstrate relatively low T_c (1.67–14 K) in these 2D metal borides with the superconducting mechanisms categorized to the coupling between (i) out-of-plane vibrational modes and electrons of boron layers (rect-GaB_6, rect-InB_6, AlB_6, MgB_6, and Li_2B_7) [28–31], (ii) vibrational modes and electrons of metal atoms (Mo_2B_2) [32], and (iii) vibrational modes of metal atoms and electron of boron atoms (hex-InB_6) [29].

*These authors contributed equally to this work.
†xml@calypso.cn
‡yinwei_li@jsnu.edu.cn
§yanggc468@nenu.edu.cn

Recently, structure predictions show that boron can react with manganese (Mn) with the formation of several stoichiometric 2D compounds and various properties [33,34]. Here, we have performed a systematic structure prediction on Mn-B systems to search new boron frameworks and we have uncovered a low-lying hexagonal structure for MnB_3 (h-MnB_3), which contains an intriguing boron kagome lattice. EPC calculations show relatively high superconductivity at 24.9 K for h-MnB_3, which is much higher than 2.9 K in t-MnB_3. A unique superconducting mechanism in h-MnB_3 is uncovered: the coupling of in-plane vibrational modes of boron kagome layers and electrons of Mn atoms. Further studies show that the T_c of h-MnB_3 is up to 34 K at a strain of 2% owing to the softening of in-plane modes of boron kagome layers.

II. METHODS

Structure searches of the 2D Mn-B compounds are carried out with the maximum of four formula units (f.u.) for each stoichiometry by using the swarm-intelligence based CALYPSO method [35,36], which is designed to search for the most stable or metastable structures of the given chemical composition [3,37–43]. In the process of structure prediction, the local optimizations of generated structures were performed by using the conjugate gradient method as implemented in the Vienna *ab initio* simulations code VASP [44]. The Perdew-Burke-Ernzerhof generalized gradient approximation is chosen for the exchange-correlation functional [45]. The electron-ion interaction is described by the projector augmented-wave potentials [46] with $3d^6\,4s^1$ and $3s^2\,3p^1$ configurations treated as the valence electrons for Mn and B, respectively. The phonon spectrum and EPC are calculated within the framework of the linear-response theory through the QUANTUM ESPRESSO code [47]. Ultrasoft pseudopotentials for Mn and B elements are used with a kinetic cutoff energy of 90 Ry. A q mesh of 10 $\times$ 10 and a k mesh of 40 $\times$ 40 in the first Brillouin zone are used in the EPC calculations for h-MnB_3. The T_c values are calculated using the Allen and Dynes modified McMillan equation [48]. Further computational details are given in the Supplemental Material [49].

III. RESULTS AND DISCUSSIONS

By using the CALYPSO method, we identified a hexagonal structure for MnB_3 with space group P- 3m 1 (denoted as h-MnB_3 hereafter) that is energetically slightly higher (0.08 eV/atom) than the known t-MnB_3 [34]. Similar to t-MnB_3, h-MnB_3 contains two boron layers sandwiched by Mn atoms. However, different from the linear arrangements of boron hexagons or triangles in t-MnB_3, every six boron triangles in h-MnB_3 connect by sharing atoms to construct a hexagon, forming the typical kagome lattice (Fig. 1). From the top view, Mn atoms are located at the center of each boron hexagon. The optimized structural parameters are listed in Table I.

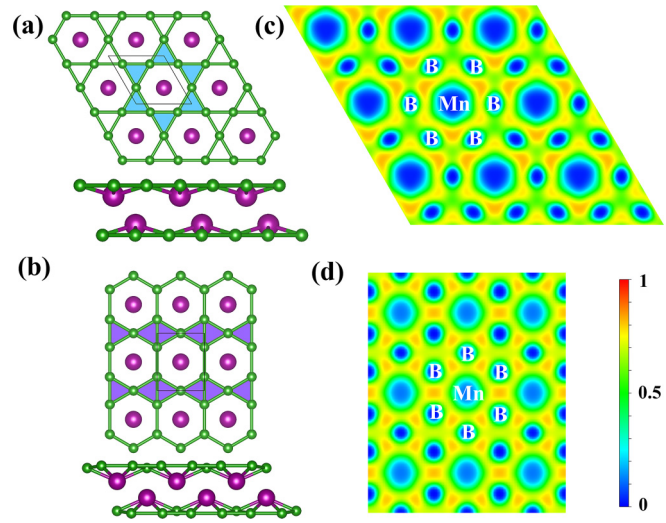

FIG. 1. Optimized crystal structures for (a) h-MnB_3 and (b) t-MnB_3. 2D maps of ELF for (c) h-MnB_3 and (d) t-MnB_3.

h-MnB_3 and t-MnB_3 contain strong covalent B-B bonds with average bond lengths of 1.91 and 1.83 Å, respectively, as also confirmed by electron localization function (ELF) calculations [Figs. 1(c) and 1(d)]. Each Mn atom connects with six B atoms in both structures with Mn-B distances of 1.98 Å in h-MnB_3 and 2.05 Å in t-MnB_3. ELF results also reveal slightly stronger covalent Mn-B bonds in h-MnB_3 as compared to t-MnB_3. Additionally, Bader analysis shows 0.35 e charges transferred from each Mn atom to the boron kagome layer. In fact, pure boron kagome layers are found to be dynamically unstable due to the electron deficiency of boron [28]. We therefore conclude that the captured electrons from Mn atoms and the formation of the covalent Mn-B bonds stabilize the boron kagome layers.

A previous study has shown that t-MnB_3 is nonmagnetic [34]. To study the magnetism of h-MnB_3, we have calculated the energy difference between different magnetic states and nonmagnetic states. As shown in Fig. S1 in the Supplemental Material [49], four possible magnetic configurations [one ferromagnetic (FM) and three antiferromagnetic (AFM)] were considered in the calculations. Results indicate that h-MnB_3 in the four magnetic states has the same energies as that of

TABLE I. Optimized lattice parameters and atomic positions for h-MnB_3 and t-MnB_3.

Phases	Space group	Lattice parameters (Å)	Atomic position
h-MnB_3	P-3m 1	$a = 3.82$	Mn (2d) (0.333, 0.667, 0.467)
			B (6i) (0.339, 0.170, 0.443)
t-MnB_3	$Pmmn$	$a = 3.70$	Mn (2a) (0, 0, 0.471)
		$b = 3.05$	B1 (2b) (0, 0.5, 0.575)
			B2 (4f) (0.241, 0, 0.583)

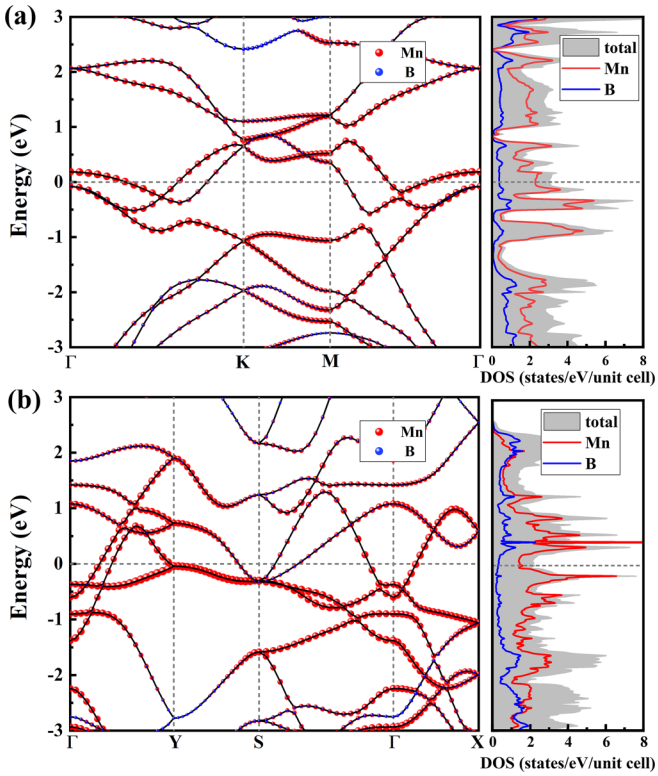

FIG. 2. Atom-resolved band structures and PDOS for (a) h-MnB_3 and (b) t-MnB_3. The Fermi energy level is set to zero.

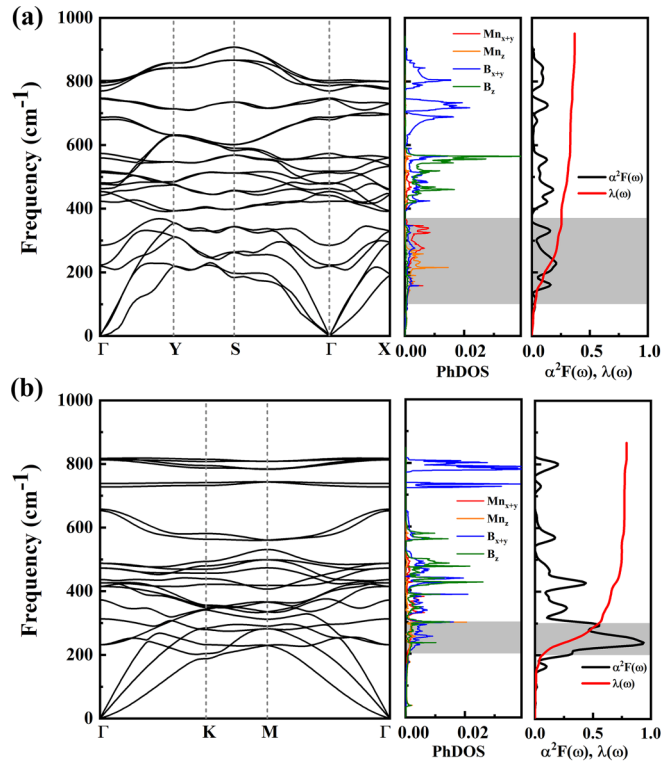

FIG. 3. Phonon dispersions, phonon density of states (PhDOS), Eliashberg function $\alpha^2F(\omega)$, and integrated electron-phonon coupling strength $\lambda(\omega)$ of (a) t-MnB_3 and (b) h-MnB_3

the nonmagnetic state. Moreover, the magnetic moment of each Mn atom is calculated to be zero in the four considered magnetic phases. Therefore, we conclude that h-MnB_3 is also nonmagnetic.

The cohesive energy (E_{coh}) is a useful parameter to evaluate the possible synthesis of a predicted 2D material [50,51]. The E_{coh} of MnB_3 is calculated according to the following equation:

$$E_{coh} = \left(E_{MnB_3} - E_{Mn} - 3E_B\right)/(N_{Mn} + N_B),$$

where E_{MnB_3} is the total energy of MnB_3, and E_{Mn} and E_B are the energies of bulk magnetic hcp Mn and 2D β_{12} boron, respectively. We choose 2D β_{12} boron as the reference since it has been synthesized in experiment. As shown in Fig. S2 [49], although h-MnB_3 is metastable with higher energies (0.08 eV/atom) than that of t-MnB_3, it has a negative cohesive energy of −0.25 eV/atom, indicating the possibility for synthesis.

The orbital-resolved band structures and density of states (DOS) of h-MnB_3 and t-MnB_3 are presented in Fig. 2. We find that both phases exhibit intrinsic metallic features with several bands crossing the Fermi energy. We have also calculated the band structure of h-MnB_3 using QUANTUM ESPRESSO. As shown in Fig. S3 in the Supplemental Material [49], the band structures calculated using two codes are consistent, confirming the accuracy of our results. It is worth noting that the band structure remains nearly unchanged when the spin-orbit coupling is considered, indicating that the spin-orbit effect is very weak in h-MnB_3 (Fig. S4 [49]). Therefore, the spin-orbit effect is ignored in the following calculations. Both orbital-resolved band structures and partial DOS results show that the electrons near the Fermi level are mainly from Mn atoms, while the contribution from B atoms is negligible. The total DOS at Fermi level in h-MnB_3 is calculated to be 1.53 states/eV/f.u., much higher than that (1.15 states/eV/f.u.) in t-MnB_3. More electrons at the Fermi level raise the possibility of the formation of Cooper pairs in h-MnB_3, which is the key to increasing electron-phonon coupling.

Figure 3 presents the calculated phonon dispersions and projected phonon density of states of h-MnB_3 and t-MnB_3. Dynamical stabilities are evidenced by the absence of imaginary frequencies in the whole Brillouin zone for the two phases. In t-MnB_3, the vibration modes are divided into three parts, the low-frequency (0−400 cm^{-1}) Mn vibrations, the midfrequency (400−600 cm^{-1}) B_{x+y} (vibrations in the x-y plane) and B_z (vibrations out of the x-y plane) vibrations, and the high-frequency (>600 cm^{-1}) B_{x+y} vibrations. The vibration modes in h-MnB_3 can be classified into two parts, with low frequencies (0−550 cm^{-1}) contributed by mixing of B and Mn vibrations, while the high ends are dominated only by B vibrations. In the low-frequency range of 200−300 cm^{-1}, we find totally opposite vibration modes for h-MnB_3 and t-MnB_3, with dominant in-plane vibrations of boron kagome and Mn vibrations, respectively. The following analysis shows this difference leads to different superconductivity in the two phases.

The T_c is calculated based on the Allen-Dynes modified McMillian equation, where μ^* can be estimated according to the equation $\mu^* \approx 0.26\ N_{E_f}/(1+\ N_{E_f})$, where N_{E_f} is the

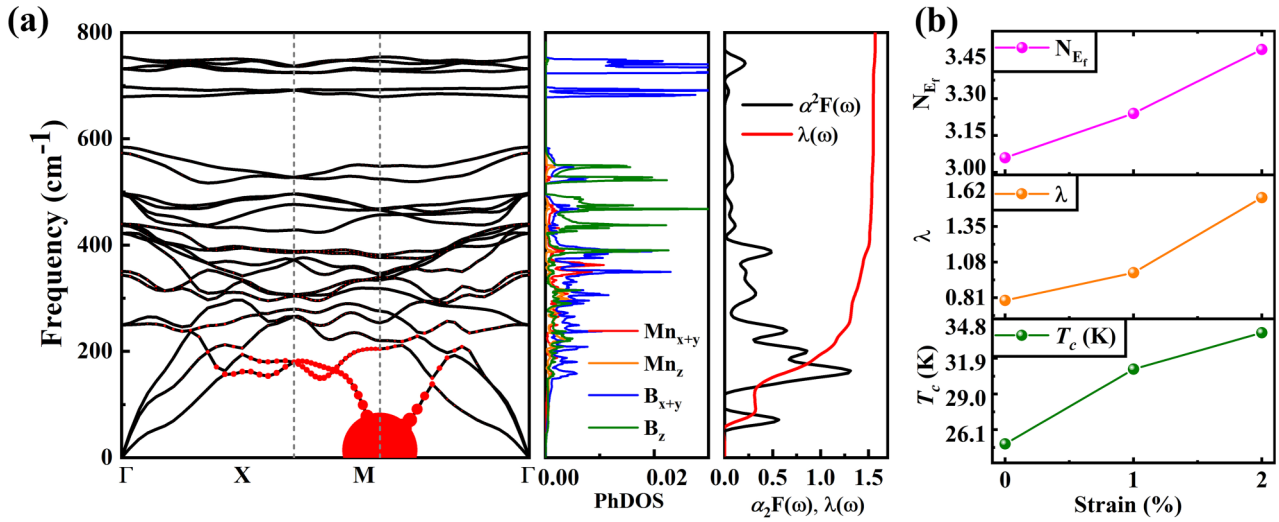

FIG. 4. (a) Phonon dispersion, phonon density of states (PhDOS), Eliashberg function $\alpha^2F(\omega)$, and integrated electron-phonon coupling strength $\lambda(\omega)$ in h-MnB_3 under strain =2%. The phonon dispersion is decorated with red ribbons, proportional to the partial electron-phonon coupling strength, λ_{qv}. (b) Biaxial strain effects on N_{E_f}, λ, and T_c of h-MnB_3.

electronic density of states at the Fermi level [52]. Based on this equation, the estimated value of μ^* is ~ 0.05 for h-MnB_3 and t-MnB_3. Moreover, considering that $\mu^* = 0.05$ has been used to estimate T_c of 2D boron allotropes [27], we therefore choose the same value for the convenience of comparison. The calculated EPC parameter λ for t-MnB_3 and h-MnB_3 is 0.37 and 0.79, resulting in T_c of 2.9 and 24.9 K, respectively. We have also estimated the T_cs of t-MnB_3 and h-MnB_3 with the choice of different μ^*. As shown in Fig. S5 in the Supplemental Material [49], T_c decreases with increasing μ^*. For example, T_c of h-MnB_3 decreases from 25 K with $\mu^* = 0.05$ to 15 K with $\mu^* = 0.13$.

Figure 3 also presents the Eliashberg spectral function $a^2F(\omega)$ and the integrated EPC strength $\lambda(\omega)$ for both phases. Obviously, the superconductivity in h-MnB_3 mainly originates from the low frequencies in the range of 200−300 cm^{-1}, which contribute 62% to the total λ. Intriguingly, these frequencies are dominated by the in-plane vibrations of B atoms in kagome layers. Considering the large DOS at the Fermi level from Mn atoms, we therefore conclude that the coupling between electrons of Mn atoms and in-plane phonons of boron kagome induces high superconductivity in h-MnB_3. This mechanism is different from those found in all other 2D borides [28–33]. Previous study has also demonstrated another boron kagome containing 2D MgB_6, which possesses a relatively low T_c of 4.7 K [28]. In fact, different from h-MnB_3, the superconductivity in MgB_6 is driven by the coupling between electrons and phonons of B atoms, and the absence of Mg contribution to EPC leads to relatively low T_c [28].

For t-MnB_3, it is found that the low–frequency (100−370 cm^{-1}) vibrations contribute 61% to the total λ; they are dominated by Mn vibrations. This phenomenon indicates that the superconductivity is driven by the coupling between electrons and vibrations of Mn atoms. The superconducting mechanism in t-MnB_3 is similar to Mo_2B_2, which also has low superconductivity at 3.9 K [32]. The low superconductivity in t-MnB_3 is understandable since the light element boron is almost not involved in the electron-phonon coupling.

Studies have demonstrated that tensile strain is effective to regulate the superconductivity of a given compound by changing its electronic and dynamical properties [15,32,53–57]. Phonon calculations reveal that h-MnB_3 remains dynamically stable under a maximum biaxial strain of 2%, above which h-MnB_3 becomes unstable in view of the presence of imaginary frequencies. Interestingly, we found that tensile strain increases λ with a maximum value reaching as high as 1.56 at the 2% strain, leading to an obviously increased T_c of 34 K.

The significant increase of λ in h-MnB_3 is understandable if we include the change of electronic and dynamical properties under tensile strain. Electronic calculations show that the DOS at the Fermi level (N_{E_f}) increases from 1.53 states/eV/f.u. in the intrinsic phase to 1.75 states/eV/f.u. at the 2% strain, providing more electrons that form Cooper pairs. Simultaneously, tensile strain induces a softened acoustic frequency at the M point in the range of 0−100 cm^{-1} [Fig. 4(a)], leading to a new step of $\lambda(\omega)$ around 100 cm^{-1}, which contributes ∼20% to the total λ [right panel in Fig. 4(a)]. Analysis suggests that the softened modes in h-MnB_3 are mainly contributed by the in-plane vibrations of boron kagome, which are believed to increase the electron-phonon pairing potential at the Fermi level, which is essential to enhance the EPC. Similar behavior was also suggested in enhanced superconductivity in strain-applied graphene [57].

Generally, metastable 2D materials are able to be synthesized through proper substrates. For example, both β^{12} and χ_3 phases of 2D boron sheets are metastable, which are energetically higher (∼0.05 eV/atom) than that of the ground state 2D α'-sheet B structure; they have been successfully synthesized using an Ag(111) substrate [58,59]. Owing to relatively high superconductivity of h-MnB_3, it is necessary to explore the possibility of experimental synthesis. Here, we selected Si as the substrate for the h-MnB_3 monolayer since the Si (111) surface has relatively small lattice mismatch of 0.46% with h-MnB_3 (shown in Fig. S6 [49]). To quantitatively describe the interaction between the Si(111) substrate and

the h-MnB_3 monolayer, the interfacial cohesive energies (E_I) of h-MnB_3 on the Si(111) surface have been calculated as follows,

$$E_I = \left(E_{sub} + E_{MnB_3} - E_{tot}\right)/(N_{Mn} + N_B),$$

where E_{sub}, E_{MnB_3}, and E_{tot} are the total energies of the Si(111) substrate, the h-MnB_3 monolayer, and the h-MnB_3 monolayer on the Si(111) surface, respectively. The calculated E_I is 0.13 eV/atom, which is comparable to that (0.3 eV/atom) of metastable β_{12} and χ_3 boron sheets on Ag substrates [60]. Therefore, it is highly possible to synthesize h-MnB_3 on a Si(111) substrate.

It is notable that the superconductivity of 2D materials could be affected by substrates due to the interfacial interaction. For example, the superconductivity of the β_{12} 2D boron sheet is significantly suppressed when considering the effect of Ag(111) substrate due to the large lattice mismatch (2%) [55]. In the case of h-MnB_3/Si (111), the lattice mismatch is found to be only 0.46%. Significantly, the band structure of free-standing h-MnB_3 can be well retained on the substrate (Fig. S6 [49]). Thus, we can expect that the superconductivity of h-MnB_3 is robust against the substrate of Si.

IV. CONCLUSION

In summary, based on first-principles calculations with structure searching, we have identified a unique low-energy hexagonal h-MnB_3 monolayer consisting of two boron kagome layers. Electron-phonon coupling calculation indicates that h-MnB_3 has intrinsic superconductivity with a high T_c of 24.9 K, higher than most 2D borides. Our analysis indicates that the boron kagome lattice contributes significantly to the superconductivity, which is attributed to the coupling between in-plane vibrational phonons of boron kagome layers and electrons of Mn atoms. We also demonstrated that the tensile strain enhances significantly the EPC of h-MnB_3, the T_c of which increases to 34 K at 2% tensile strain. Additionally, we conclude that a Si (111) surface may be an ideal substrate for the growth of superconductive h-MnB_3. Our results suggest that borides with a unique boron kagome lattice are promising superconductors.

ACKNOWLEDGMENTS

Y.L. and M.X. acknowledge funding from the National Natural Science Foundation of China under Grants No. 11722433 and No. 11904142. Z.Q. acknowledges the funding from the Postgraduate Research & Practice Innovation Program of Jiangsu Province under Grant No. KYCX20_2226. G.Y. acknowledges funding from the National Natural Science Foundation of China under Grants No. 21873017 and No. 21573037. All the calculations were performed using the High Performance Computing Center of the School of Physics and Electronic Engineering of Jiangsu Normal University.

The authors declare no competing financial or nonfinancial interests.

[1] H. Wang, X. Li, G. Gao, Y. Li, and Y. Ma, WIREs Comput. Mol. Sci. **8**, e1330 (2018).
[2] E. Zurek and T. Bi, J. Chem. Phys. **150**, 050901 (2019).
[3] Y. Li, J. Hao, H. Liu, Y. Li, and Y. Ma, J. Chem. Phys. **140**, 174712 (2014).
[4] D. Duan, Y. Liu, F. Tian, D. Li, X. Huang, Z. Zhao, H. Yu, B. Liu, W. Tian, and T. Cui, Sci. Rep. **4**, 6968 (2015).
[5] F. Peng, Y. Sun, C. J. Pickard, R. J. Needs, Q. Wu, and Y. Ma, Phys. Rev. Lett. **119**, 107001 (2017).
[6] Y. Sun, J. Lv, Y. Xie, H. Liu, and Y. Ma, Phys. Rev. Lett. **123**, 097001 (2019).
[7] A. P. Drozdov, M. I. Eremets, I. A. Troyan, V. Ksenofontov, and S. I. Shylin, Nature **525**, 73 (2015).
[8] M. Einaga, M. Sakata, T. Ishikawa, K. Shimizu, M. I. Eremets, A. P. Drozdov, I. A. Troyan, N. Hirao, and Y. Ohishi, Nat. Phys. **12**, 835 (2016).
[9] M. Somayazulu, M. Ahart, A. K. Mishra, Z. M. Geballe, M. Baldini, Y. Meng, V. V. Struzhkin, and R. J. Hemley, Phys. Rev. Lett. **122**, 027001 (2019).
[10] A. P. Drozdov, P. P. Kong, V. S. Minkov, S. P. Besedin, M. A. Kuzovnikov, S. Mozaffari, L. Balicas, F. F. Balakirev, D. E. Graf, V. B. Prakapenka, E. Greenberg, D. A. Knyazev, M. Tkacz, and M. I. Eremets, Nature **569**, 528 (2019).
[11] S. Ichinokura, Y. Nakata, K. Sugawara, Y. Endo, A. Takayama, T. Takahashi, and S. Hasegawa, Phys. Rev. B **99**, 220501(R) (2019).
[12] G. Profeta, M. Calandra, and F. Mauri, Nat. Phys. **8**, 131 (2012).
[13] E. Navarro-Moratalla, J. O. Island, S. Mañas-Valero, E. Pinilla-Cienfuegos, A. Castellanos-Gomez, J. Quereda, G. Rubio-Bollinger, L. Chirolli, J. A. Silva-Guillén, N. Agraït, G. A. Steele, F. Guinea, H. S. J. van der Zant, and E. Coronado, Nat. Commun. **7**, 11043 (2016).
[14] X. Xi, Z. Wang, W. Zhao, J.-H. Park, K. T. Law, H. Berger, L. Forró, J. Shan, and K. F. Mak, Nat. Phys. **12**, 139 (2016).
[15] Q. Wu, J.-J. Zhang, P. Hao, Z. Ji, S. Dong, C. Ling, Q. Chen, and J. Wang, J. Phys. Chem. Lett. **7**, 3723 (2016).
[16] X. Zhang, Y. Zhou, B. Cui, M. Zhao, and F. Liu, Nano Lett. **17**, 6166 (2017).
[17] J.-J. Zhang and S. Dong, J. Chem. Phys. **146**, 034705 (2017).
[18] B.-T. Wang, P.-F. Liu, T. Bo, W. Yin, O. Eriksson, J. Zhao, and F. Wang, Phys. Chem. Chem. Phys. **20**, 12362 (2018).
[19] B. M. Ludbrook, G. Levy, P. Nigge, M. Zonno, M. Schneider, D. J. Dvorak, C. N. Veenstra, S. Zhdanovich, D. Wong, P. Dosanjh, C. Straßer, A. Stöhr, S. Forti, C. R. Ast, U. Starke, A. Damascelli, and J. C. Séamus Davis, Proc. Natl. Acad. Sci. USA **112**, 11795 (2015).
[20] J. Bekaert, L. Bignardi, A. Aperis, P. van Abswoude, C. Mattevi, S. Gorovikov, L. Petaccia, A. Goldoni, B. Partoens, P. M. Oppeneer, F. M. Peeters, M. V. Milošević, P. Rudolf, and C. Cepek, Sci. Rep. **7**, 14458 (2017).
[21] J. Miller, Phys. Today **60**(8), 19 (2007).
[22] H. Tang and S. Ismail-Beigi, Phys. Rev. Lett. **99**, 115501 (2007).
[23] C. Özdoğan, S. Mukhopadhyay, W. Hayami, Z. B. Güvenç, R. Pandey, and I. Boustani, J. Phys. Chem. C **114**, 4362 (2010).

[24] H. Tang and S. Ismail-Beigi, Phys. Rev. B **82**, 115412 (2010).
[25] E. S. Penev, S. Bhowmick, A. Sadrzadeh, and B. I. Yakobson, Nano Lett. **12**, 2441 (2012).
[26] E. S. Penev, A. Kutana, and B. I. Yakobson, Nano Lett. **16**, 2522 (2016).
[27] Y. Zhao, S. Zeng, and J. Ni, Phys. Rev. B **93**, 014502 (2016).
[28] S. Y. Xie, X. Bin Li, W. Q. Tian, N. K. Chen, Y. Wang, S. Zhang, and H. B. Sun, Phys. Chem. Chem. Phys. **17**, 1093 (2015).
[29] L. Yan, T. Bo, P. F. Liu, L. Zhou, J. Zhang, M. H. Tang, Y. G. Xiao, and B. T. Wang, J. Mater. Chem. C **8**, 1704 (2020).
[30] C. Wu, H. Wang, J. Zhang, G. Gou, B. Pan, and J. Li, ACS Appl. Mater. Interfaces **8**, 2526 (2016).
[31] B. Song, Y. Zhou, H.-M. Yang, J.-H. Liao, L.-M. Yang, X.-B. Yang, and E. Ganz, J. Am. Chem. Soc. **141**, 3630 (2019).
[32] L. Yan, T. Bo, P.-F. Liu, B.-T. Wang, Y.-G. Xiao, and M.-H. Tang, J. Mater. Chem. C **7**, 2589 (2019).
[33] M. U. Farooq, A. Hashmi, I. Khan, and J. Hong, Sci. Rep. **7**, 17101 (2017).
[34] X. Zhang, Z. Zhang, X. Zhao, D. Wu, and Z. Zhou, FlatChem **4**, 42 (2017).
[35] Y. Wang, M. Miao, J. Lv, L. Zhu, K. Yin, H. Liu, and Y. Ma, J. Chem. Phys. **137**, 224108 (2012).
[36] Y. Wang, J. Lv, L. Zhu, S. Lu, K. Yin, Q. Li, H. Wang, L. Zhang, and Y. Ma, J. Phys.: Condens. Matter **27**, 203203 (2015).
[37] W. Cui and Y. Li, Chin. Phys. B **28**, 107104 (2019).
[38] J. Lv, M. Xu, S. Lin, X. Shao, X. Zhang, Y. Liu, Y. Wang, Z. Chen, and Y. Ma, Nano Energy **51**, 489 (2018).
[39] Y. Li, X. Feng, H. Liu, J. Hao, S. A. T. Redfern, W. Lei, D. Liu, and Y. Ma, Nat. Commun. **9**, 722 (2018).
[40] Y. Li, L. Wang, H. Liu, Y. Zhang, J. Hao, C. J. Pickard, J. R. Nelson, R. J. Needs, W. Li, Y. Huang, I. Errea, M. Calandra, F. Mauri, and Y. Ma, Phys. Rev. B **93**, 020103(R) (2016).
[41] Y. Li, Y. Wang, C. J. Pickard, R. J. Needs, Y. Wang, and Y. Ma, Phys. Rev. Lett. **114**, 125501 (2015).
[42] Y. Li, J. Hao, H. Liu, S. Lu, and J. S. Tse, Phys. Rev. Lett. **115**, 105502 (2015).
[43] Y. Li, J. Hao, H. Liu, J. S. Tse, Y. Wang, and Y. Ma, Sci. Rep. **5**, 9948 (2015).
[44] G. Kresse and J. Furthmüller, Phys. Rev. B **54**, 11169 (1996).
[45] J. P. Perdew, K. Burke, and M. Ernzerhof, Phys. Rev. Lett. **77**, 3865 (1996).
[46] G. Kresse and D. Joubert, Phys. Rev. B **59**, 1758 (1999).
[47] P. Giannozzi, S. Baroni, N. Bonini, M. Calandra, R. Car, C. Cavazzoni, D. Ceresoli, G. L. Chiarotti, M. Cococcioni, I. Dabo, A. Dal Corso, S. de Gironcoli, S. Fabris, G. Fratesi, R. Gebauer, U. Gerstmann, C. Gougoussis, A. Kokalj, M. Lazzeri, and L. Martin-Samos *et al.*, J. Phys.: Condens. Matter **21**, 395502 (2009).
[48] P. B. Allen and R. C. Dynes, Phys. Rev. B **12**, 905 (1975).
[49] See Supplemental Material at http://link.aps.org/supplemental/10.1103/PhysRevB.102.075431 for more details on the structure prediction, possible magnetic configurations, the effect of Si substrate on the electronic band structure of h-MnB_3, spin-orbit effect, and T_cs with different μ^*.
[50] T. Yu, Z. Zhao, L. Liu, S. Zhang, H. Xu, and G. Yang, J. Am. Chem. Soc. **140**, 5962 (2018).
[51] H. Zhang, Y. Li, J. Hou, K. Tu, and Z. Chen, J. Am. Chem. Soc. **138**, 5644 (2016).
[52] K. H. Bennemann and J. W. Garland, in *Superconductivity in d- and f- bands Metals*, edited by H C. Wolfe and D. H. Douglass, AIP Conf. Proc. No. 4 (AIP, Melville, 1972), p. 103.
[53] R. C. Xiao, D. F. Shao, W. J. Lu, H. Y. Lv, J. Y. Li, and Y. P. Sun, Appl. Phys. Lett. **109**, 122604 (2016).
[54] Z. Qu, S. Lin, M. Xu, J. Hao, J. Shi, W. Cui, and Y. Li, J. Mater. Chem. C **7**, 11184 (2019).
[55] C. Cheng, J.-T. Sun, H. Liu, H.-X. Fu, J. Zhang, X.-R. Chen, and S. Meng, 2D Mater. **4**, 025032 (2017).
[56] Y. Ge, W. Wan, F. Yang, and Y. Yao, New J. Phys. **17**, 035008 (2015).
[57] C. Si, Z. Liu, W. Duan, and F. Liu, Phys. Rev. Lett. **111**, 196802 (2013).
[58] B. Feng, J. Zhang, Q. Zhong, W. Li, S. Li, H. Li, P. Cheng, S. Meng, L. Chen, and K. Wu, Nat. Chem. **8**, 563 (2016).
[59] A. J. Mannix, X.-F. Zhou, B. Kiraly, J. D. Wood, D. Alducin, B. D. Myers, X. Liu, B. L. Fisher, U. Santiago, J. R. Guest, M. J. Yacaman, A. Ponce, A. R. Oganov, M. C. Hersam, and N. P. Guisinger, Science **350**, 1513 (2015).
[60] H. Shu, F. Li, P. Liang, and X. Chen, Nanoscale **8**, 16284 (2016).